Direct comparison of density-driven convective mixing in a three-dimensional porous medium using experiments and simulation

Rebecca Liyanage [1,*] Xiaojing Fu,[2,†] Ronny Pini [3] and Ruben Juanes [4,‡]

[1]*Universite de Pau et des Pays de l'Adour, E2S UPPA, DMEX, Pau, France*
[2]*Department of Mechanical and Civil Engineering, California Institute of Technology, Pasadena, California 91125, USA*
[3]*Department of Chemical Engineering, Imperial College London, London, United Kingdom*
[4]*Department of Civil and Environmental Engineering, Massachusetts Institute of Technology, Cambridge, Massachusetts 02139, USA*

We perform a direct comparison between experiment and simulation of density-driven convective mixing in three-dimensional (3D) porous media. We find excellent agreement between the experiment and the model in terms of both the convection fingering pattern and the average rate of fluid mixing. In particular, the experiment exhibits dynamic self-organization of columnar plumes into a reticular pattern, which, until now, had only been observed in 3D simulations. We also report good quantitative agreement between the experiment and simulation in the evolution of the state of mixing by comparing, over time, (i) the average concentration at depth, (ii) the variance of the concentration field, (iii) the scalar dissipation rate, and (iv) the dissolution flux. We derive a relation between the scalar dissipation rate and the dissolution flux in a closed system, and we show that the flux in a 3D system is approximately ~30% higher than in a 2D system, confirming previous numerical estimates.

I. INTRODUCTION

Density-driven convective mixing of two miscible fluids in porous media is initiated by local perturbations at a stable fluid-fluid interface due to an unfavorable density contrast upon mixing. The subsequent fluid mechanical instability results in the formation and growth of fingered flow. The downward movement of the more dense fingers induces a convective overturn in the underlying fluid, accelerating the mixing of the two fluids compared to the diffusion-only scenario. This process is relevant in many natural and engineered systems [1], and one of its earliest applications is convection sustained by geothermal activity [2], which is the thermal analog of solutal convection. In the past two decades, density-driven convective mixing has received renewed attention due to its application in geological sequestration of carbon dioxide (CO_2) [3,4], which aims to mitigate climate change by storing captured CO_2 underground in suitable geological formations.

A large body of work has used two-dimensional (2D) numerical simulations to characterize the evolution of the flow dynamics [4–8], and the effect of fluid properties [9,10], dispersion [11–14], and permeability heterogeneity [15,16] on flow. In parallel to these modeling efforts, experimental studies have used Hele-Shaw cells [17–19] or pseudo-2D cells filled with glass beads

---

*rebecca.liyanage@univ-pau.fr

†rubyfu@caltech.edu

‡juanes@mit.edu

to visualize and quantify the flow patterns. These experiments are often done with analog miscible fluid-pairs (e.g., methanol and ethylene glycol-water [20,21]), water-propylene glycol [17,22–24], or partially miscible fluid pairs (e.g., gaseous CO_2-water [25]), or a solid-liquid pair (e.g., potassium permanganate in water [26,27]). More recent experiments have used the CO_2-brine systems in a pressure-volume-temperature cell [28–32] and incorporated permeability heterogeneity [22,33,34] to mimic more closely the subsurface environment. Only a handful of studies have addressed this problem in 3D using either experiments [35–40] or simulations [16,41–43].

The convective mixing process in porous media is, however, inherently three-dimensional. Whether conclusions from 2D studies can be readily applied to the 3D problem remains insufficiently addressed in the literature. Despite the demanding computational cost in 3D, there has been a handful of numerical studies that examine convective mixing in 3D [16,41–48]. In particular, both Pau *et al.* [41] and Fu *et al.* [43] have concluded that the flux calculated in 3D simulations is about 30% larger than that obtained from 2D simulations. Their conclusions highlight the necessity to validate results obtained from 2D experiments and simulations in 3D settings. However, direct observations of density-driven convective mixing in 3D porous media are limited, because of the experimental challenges associated with probing this process in opaque media. In recent work, x-ray computed tomography (x-ray CT) and the MEG-brine fluid pair were used to visualize convection in a 3D cylindrical cell [35,49] and a spherical cell [36,37]. These 3D experiments show a remarkable qualitative resemblance in flow patterns to those from 3D simulations. However, there is a lack of direct quantitative comparison between experiment and simulation of the mixing dynamics in 3D.

In this article, we aim to bridge the gap by presenting a *quantitative* one-to-one comparison of convective mixing in 3D porous media using the methodology laid out in previous publications with x-ray CT [36] and high-resolution numerical simulation [43]. This work directly quantifies the mixing dynamics in 3D porous media using experiments and numerical simulations. Our results have shown remarkable quantitative agreement between experiment and simulation, both in terms of characteristic lengthscales of the flow patterns as well as the temporal dynamics of dissolution flux.

II. METHODOLOGY

A. Experimental setup

We use a mixture of 59 wt. % methanol and 41 wt. % ethylene glycol (MEG) containing 10 wt. % potassium iodide (KI) that allows a good x-ray contrast against the resident fluid (6 wt. % sodium chloride brine) but maintains a neutral buoyancy. The flow cell is an acrylic cube of $15 \times 15 \times 15$ cm (Fig. 1). The cube is first wet packed with brine and soda glass beads with a particle diameter of 0.4–0.5 mm (SiLibeads®, supplied by VWR, UK) to a height of $H_B \approx 13$ cm. To initiate the experiment, we introduce the MEG and glass bead slurry to create a layer with a height of $H_T \approx 2$ cm. Because it takes some time for the fluids to mix, the gravitational instability does not begin right away, which allows sufficient time to prepare for the scanning procedure. In previous studies [36,37], we show that the method is robust and not sensitive to initial perturbations. Assuming a random close packing with a porosity $\phi = 0.36$, the Kozeny-Carman equation yields a permeability of $k = 1.9 \times 10^{-10}$ m^2. A Toshiba 64-slice x-ray CT scanner noninvasively images mixing at regular time intervals. The first CT scan starts shortly after introducing the slurry. Scans were taken every minute for 10 min, after which every 10 min for 1 h, then regularly until the experiment was ended after 5 h. Each scan takes less than 1 min.

B. Mass fraction and fluid density

The above experimental system is composed of a single-phase two-component fluid, characterized by χ, the mass fraction of MEG, and ρ, the density of the solution, which is a function of χ, $\rho = \rho(\chi)$. The concentration of MEG is then defined as $c \equiv \rho(\chi) \chi$ (g/mL).
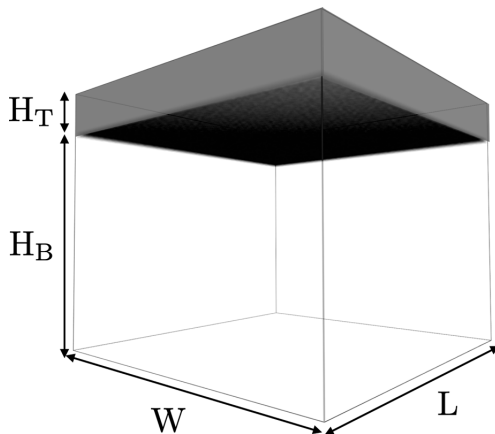
FIG. 1. A diagram that illustrates the initial setup and the dimensions of the convective dissolution problem in an enclosed cube. H_T corresponds to the initial thickness of the MEG-brine layer and H_B is the initial thickness of the MEG-free resident brine. In the experiment presented in this study, $H_T = 2$ cm, $H_B = 13$ cm, $W = L = 15$ cm.

The raw CT images are converted into a mass fraction of dissolved MEG, χ, through measured calibration curves [36]. We also experimentally measure the density profile of the MEG-brine mixture and determine that $\rho(\chi) = -0.03\chi^3 - 0.0084\chi^2 + 0.0304\chi + \rho_0$ (g/mL), where $\rho_0 = 1.04$ g/mL is the density of the MEG-free solution.

C. High-resolution 3D simulations

To compare with the experiment, we perform a high-resolution 3D simulation of the equations that govern gravity-driven convective mixing in homogeneous porous media [50]:

$$\nabla \cdot \mathbf{u} = \mathbf{0}, \tag{1}$$

$$\mathbf{u} = -\frac{k}{\mu}[\nabla p - \rho(\chi)g\hat{\mathbf{z}}], \tag{2}$$

$$\phi\frac{\partial c}{\partial t} + \nabla \cdot (\mathbf{u}c - \phi D\nabla c) = \mathbf{0}, \tag{3}$$

where $\mathbf{u}$ is the Darcy velocity, p is the fluid pressure, and $\hat{\mathbf{z}}$ is a unit vector pointing in the direction of gravity. Equations (1) and (2) are the incompressibility constraint accompanied by Darcy's law. Equation (3) is the advection-diffusion transport equation, where we assume a constant molecular diffusion coefficient $D_m = 1 \times 10^{-9}$ m^2/s [51]. The maximum viscosity difference between the two fluids is 2.5 mPa s [37]. We assume a constant viscosity $\mu = 1.09$ mPa s, which is taken as that of the resident brine [20,21,35,36].

We initialize the numerical simulation with $c = 1$ in the upper layer ($z < H_T$) and $c = 0$ in the lower layer ($z > H_T$). The transition between the two layers at $z = H_T$ takes the shape of an error function whose transition width is scaled by $\sqrt{\text{Ra}/2}$ to reflect the diffusive nature of the initial interface:

$$c_0 = \frac{1}{2} - \frac{1}{2}\text{erf}\left(\sqrt{\frac{\text{Ra}}{2}}[z - H_T - \theta(x, y)]\right). \tag{4}$$

We perturb the initial concentration by adding a randomized Gaussian white noise $\theta(x, y)$ to the transition depth H_T. The maximum magnitude of this noise is 0.02 cm, which is small compared to

$H_T = 2$ cm. The white noise is randomized on a pixel-by-pixel basis and thus does not impose any lengthscale in the x and y directions.

The boundary conditions are no-flow on the top and bottom surfaces. We assume periodicity in the x and y directions, which deviates from the experimental setup of a closed box. We find that this approximation has little impact on our analysis but significantly speeds up the computation. We initialize the concentration field with the same initial condition used in the experiment: $c(z >= 13 \text{ cm}) = \rho(\chi = 1) = 1.032$ g/mL; $c(z < 2 \text{ cm}) = 0$ g/mL. We perturb the concentration near the interface $z \approx 13$ cm with Gaussian noise [20,41,50]. We solve the equations sequentially on a $512 \times 512 \times 512$ Cartesian grid. At each step, we obtain the velocity using the stream function–vorticity formulation [52,53] with a Poisson solver [54]; then we solve Eq. (3) using sixth-order compact finite differences [55] in $\mathbf{z}$, and a pseudospectral (Fourier) discretization along the horizontal directions. We integrate in time using a third-order Runge-Kutta scheme with automatic time-step adaptation [56].

D. Rayleigh number of the study

We choose the following characteristic quantities to normalize our equations:

$$L_c = H_B, \quad \rho_c = \rho_0, \quad \Delta\rho_c = \Delta\rho_{max}, \quad k_c = k, \quad \mu_c = \mu, \quad \Delta p_c = \Delta\rho_{max}gH_B, \quad (5)$$

where H_B is the height of the initial brine layer (13 cm), $\Delta\rho_{max}$ is the maximum density difference between the MEG-brine solution and resident brine, k is the permeability of the glass bead pack, μ is the viscosity of the resident brine, and Δp_c is the characteristic pressure difference with respect to the hydrostatic datum. In our experiments, $\Delta\rho_{max} = 0.0093$ g/mL, achieved at $\chi = 0.5$ as reported in our previous work [36,37]. After normalization, the problem can now be characterized by the Rayleigh number (Ra), which computes the ratio between the rate of convection and diffusion:

$$\text{Ra} = \frac{k\Delta\rho_{max}gH_B}{\mu\phi D_m}, \quad (6)$$

where the gravitational acceleration is $g = 9.81$ m/s^2. Based on the parameter values given above, Ra ≈ 6000 for both the experiment and the simulation in our study.

III. RESULTS

In the following, we present both qualitative and quantitative comparisons between the experiment and simulation. We use the normalized concentration $c' = c/\rho_0$ to perform these analyses. The results presented here come from a direct comparison between exactly one experiment and one 3D simulation, focusing on only Ra $= 6000$. However, many more experiments using the same setup have been performed, and the results were published in earlier studies [36,37]. Additional 3D simulations at different Rayleigh numbers using the same numerical method were performed and published in [43].

A. Plume dynamics

Reconstructions of the data in 3D and 2D slices reveal the time evolution of the characteristic columnar patterns at different depths. Here we focus on the time period before fingers hit the bottom ($t < 150$ min), when their structure remains sharp and not disrupted by any returning plume. Figure 2 shows a time series of horizontal cross-sections at $z = 4$ and 8 cm, respectively. By direct visual comparison, the pattern formation as characterized by finger lengthscale and its coarsening dynamics are strikingly consistent between experiment and simulation. In the upper section ($z = 4$ cm), at early times ($t = 40$ min), the fingers are small (diameter < 1 cm) and form bright islands distributed uniformly across the plane. As time progresses, the islands merge and coarsen with regions of high concentration (red colored) marking the center of each finger. At later
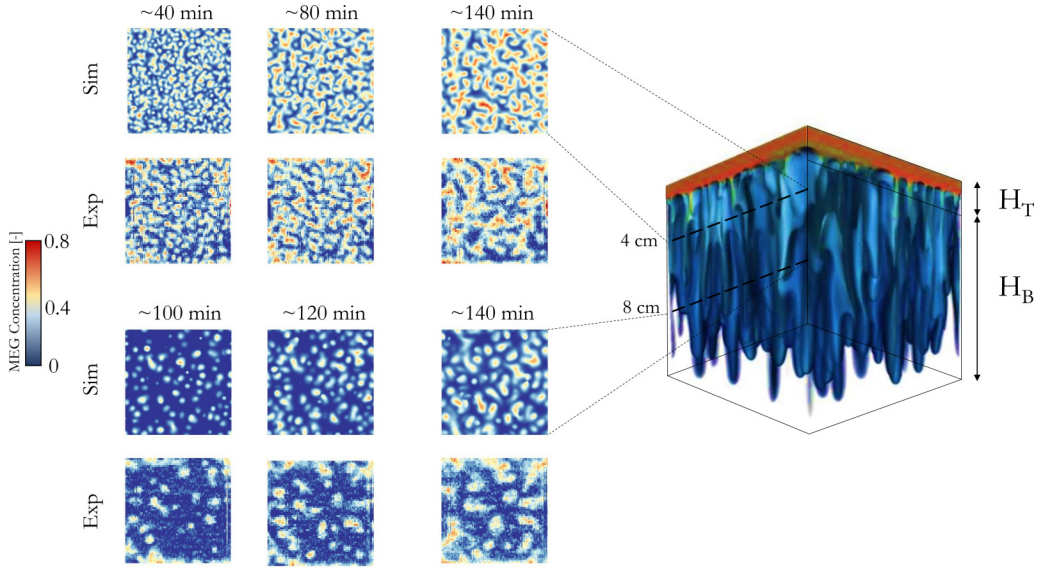
FIG. 2. Right: 3D reconstruction of the simulated c' at $t = 140$ min. Left: 2D reconstruction of fingering patterns at $z = 4$ cm and at 40, 80, and 140 min (top panel) and at $z = 8$ cm and at 100, 120, and 140 min (bottom panel). Within each panel, the top row is simulation and bottom row is experiment. Color map corresponds to the normalized MEG concentration (c').

times ($t = 140$ min), just before the fingers reach the bottom, the plumes have coarsened significantly (diameter ~5 cm) and are no longer circular. As time progresses, the fingers self-organize to become laterally connected instead of remaining as independent plumes—a feature that has been revealed by earlier 3D simulations [41,43] and has not been experimentally verified until now. The direct visual comparison is less consistent, however, in the lower section (e.g., $z = 8$ cm), where finger tips only become visible after 100 min. This is likely caused by the resolution of the CT scan and dispersion in porous media that is not considered by the simulation.

To quantify these observations in Fig. 2, for one experimental and one simulation data set, we track the time evolution of the number of fingers and average finger size at different depths (Fig. 3) by segmenting the concentration field ($c'_{\text{threshold}} = 0.2$) slice-by-slice using MATLAB, and we identify
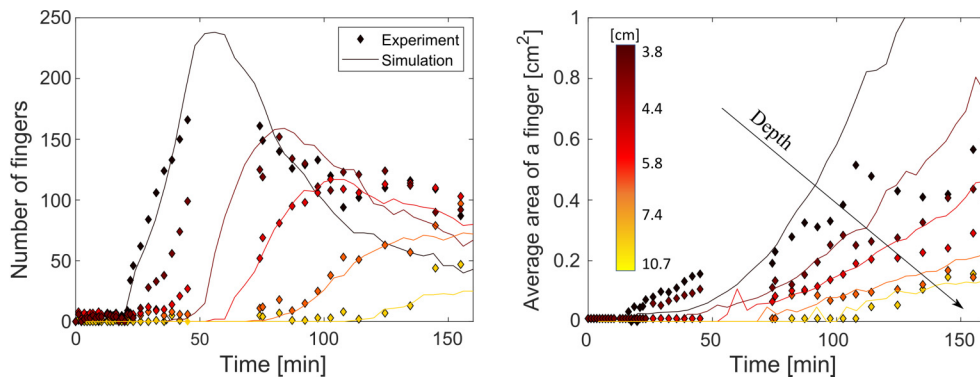

FIG. 3. The number of fingers (left) and the average area of a finger (right) for both the experiment (points) and simulation (solid lines). The results are shown at five depths where dark red is 3.8 cm, red is 4.4 cm, light red is 5.8 cm, orange is 7.4 cm, and yellow is 10.7 cm from the top.
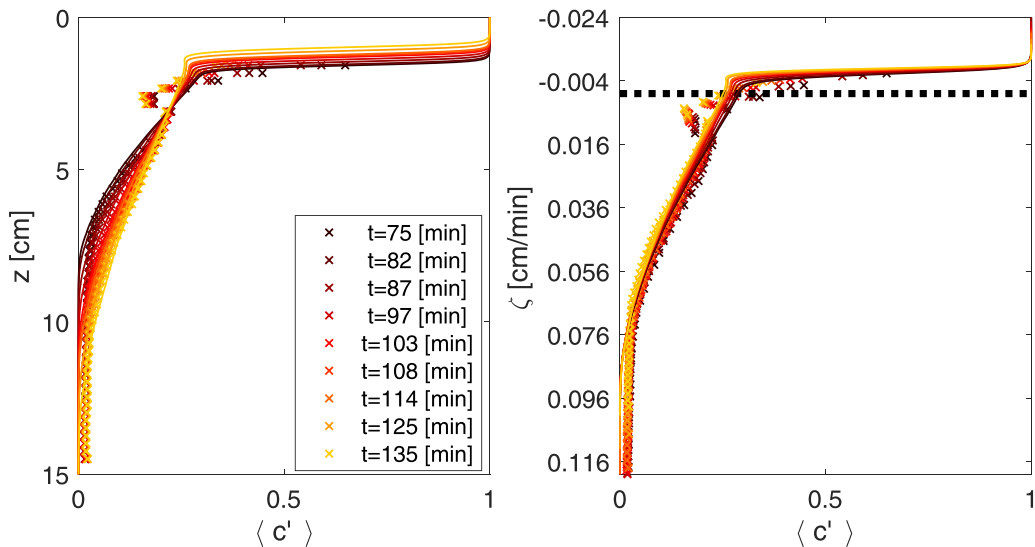
FIG. 4. Left: horizontally averaged normalized concentration $\langle c' \rangle$ over depth (z) at various times from the experiment (cross) and the simulation (solid lines). Right: the same concentration profiles plotted as a function of the self-similarity variable $\zeta = (z - z_0)/(t - t_{onset})$. The black dashed line marks $\zeta = 0$.

individual fingers. We continue to find good agreement between the experiment and simulation in these measures. The rate of finger coarsening, as measured by the slope of the curves of mean finger area over time (Fig. 3, right), decreases with increasing depth. The peak in the number of plumes decreases with depth (Fig. 3, left), indicating coarsening in both time and space [7]. This spatial-temporal coarsening can also be seen by plotting the horizontally averaged normalized concentration ($\langle c' \rangle$) over depth at various times (Fig. 4, left). Further, by replotting $\langle c' \rangle$ against the self-similarity variable $\zeta = \frac{z - z_0}{t - t_{onset}}$ [7], we are able to collapse all the curves at different times onto a master curve (Fig. 4, right). The onset time is $t_{onset} \approx 8$ min for both the experiment and the simulation. The initial interface is $z_0 = H_T = 2$ cm. The times analyzed in Fig. 4 are chosen so that the plume structure is well developed ($t \gg t_{onset}$) and not significantly impacted by the bottom boundary ($t < 150$ min). This shows that the convective mixing phenomenon in the two-layer system can also be described by self-similar dynamics at intermediate times [7].

B. Measures of mass transfer and fluid mixing

The onset and growth of these convective fingers have a profound impact on mass transfer and the rate of fluid mixing in the system. In particular, the pattern formation process accelerates downward mass transfer by invoking advection (rather than diffusion-only). Further, the fingering structure significantly increases the interfacial area of fluid mixing, thus enhancing the overall mixing rate.

Here, we directly quantify mass transport and fluid mixing in both experiment and simulation. We first plot the time evolution of the mean concentrations at different depths [Fig. 5(a)], which indirectly tracks the progression of fingering plumes as they move downward. Again, we find excellent agreement between the experiment and the simulation. Such a measure, however, only describes local dynamics and does not provide a global measure of convective mixing. One straightforward way to measure mixing by convection at the global scale is to track the total volume of mixing, defined as regions of nonzero concentration gradient at interfaces between two miscible fluids. The dimensionless mean scalar dissipation rate, defined here as $\langle \epsilon' \rangle \equiv \langle |\nabla' c'|^2 \rangle / \text{Ra}$ (∇' is the normalized gradient by H_B), is a robust measure of the mixing volume in a miscible system
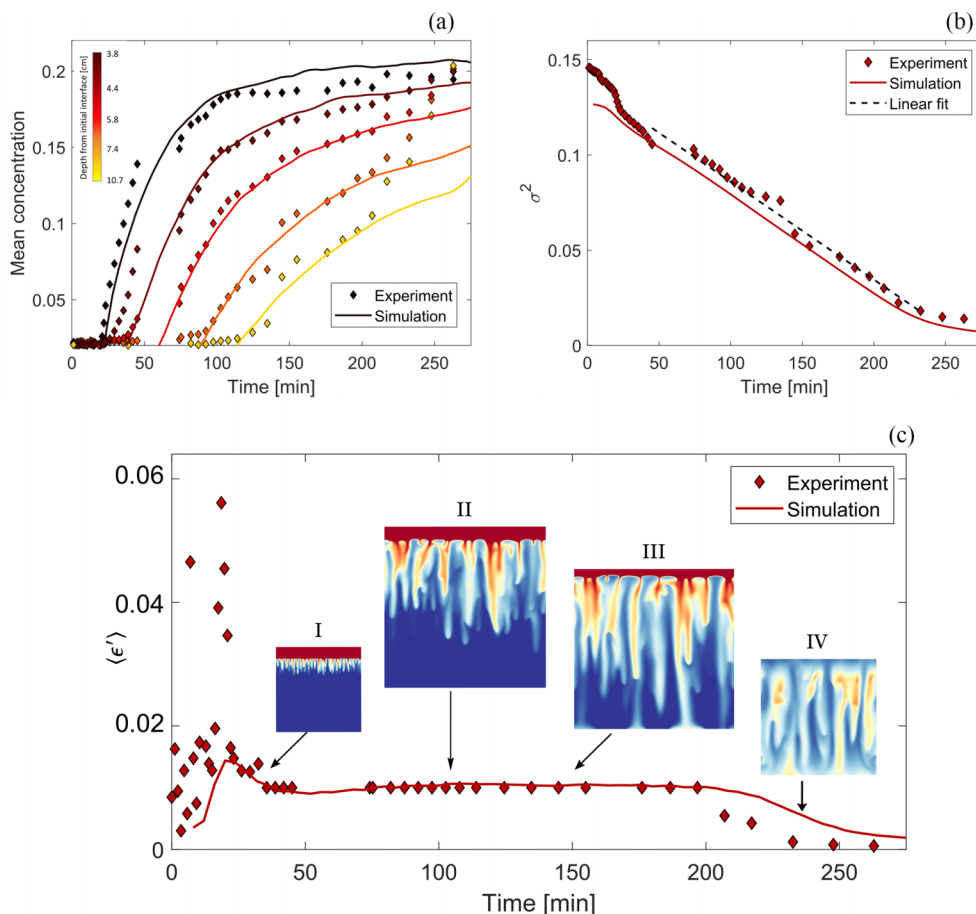
FIG. 5. (a) Mean normalized concentration over time at various depths where dark red is 3.8 cm, red is 4.4 cm, light red is 5.8 cm, orange is 7.4 cm, and yellow is 10.7 cm from the top; (b) time evolution of σ^2 and (c) time evolution of $\langle \epsilon' \rangle$ calculated from experimental images (dots) and simulation (solid lines).

[6,57,58]. We dedicate the rest of our discussion to the computation, comparison, and interpretation of ϵ' obtained from the experiment and the simulation.

With the 3D data sets in this study, $\langle \epsilon' \rangle$ can be computed directly from experimental images and simulation data. However, we find that direct computation of normalized concentration gradients ($\nabla' c'$) based on experimental images is overly sensitive to the noise inevitably introduced during CT imaging, and thus produces unreliable results. To circumvent the need for gradient calculation, we compute $\langle \epsilon' \rangle$ indirectly via the variance of the concentration field: $\sigma^2 \equiv \langle c'^2 \rangle - \langle c' \rangle^2$, where $\langle \cdot \rangle$ denotes spatial averaging over the entire volume. σ^2 quantifies the degree of mixing such that $\sigma^2 = 0$ corresponds to a perfectly mixed volume. Therefore, we expect σ^2 to decrease towards zero as the volume becomes increasingly mixed, as is confirmed by our data analysis in Fig. 5(b). Further, Fig. 5(b) illustrates that there is an excellent quantitative agreement between the experimental and simulation data without any fitting parameters. We note that σ^2 calculated from the experiment is consistently higher than the simulation by a small amount. In particular, the variance is uniformly $1.1\times$ larger in the experiment across the time series. Here, we hypothesize that the consistently higher value in the variance of the experimental data is a result of random noise from the x-ray-CT scan, which inevitably increases the variance of the measured concentration field.

While σ^2 characterizes the degree of mixing in the volume, the mean scalar dissipation rate $\langle \epsilon' \rangle$ is used to quantify the rate of mixing at a given time. As is often done in the turbulence literature [59] and more recently in the context of viscous fingering in porous media [57,58], $\langle \epsilon' \rangle$ can be calculated from the decay in σ^2:

$$\frac{\partial \sigma^2}{\partial t} = -2\langle \epsilon' \rangle. \tag{7}$$

Equation (7) provides a straightforward way to calculate $\langle \epsilon' \rangle$ as the time derivative of σ^2. In particular, to calculate $\langle \epsilon' \rangle$ from the simulation data, we use a forward Euler approximation of Eq. (7) on the simulation data in Fig. 5(b), which yields a quantity that has a unit of min^{-1}. We then multiply this quantity by the timescale of the problem $t_{scale} = 40$ min to obtain a dimensionless scalar dissipation rate. We apply the same process to the experimental data except for the data collected between $t \in [30, 200]$ min. The data collected in this time period mark a special regime of constant mixing rate that is well studied [6,26,50]. Here, taking advantage of the prior knowledge that $\langle \epsilon' \rangle$ should be constant during this period, we first impose a linear interpolation on the experimental data points in Fig. 5(b) ($t \in [30, 200]$ min) and use the slope of the linear interpolation to calculate $\langle \epsilon' \rangle$. Doing so avoids noise amplification during numerical differentiation. We do not perform any further smoothing or fitting after the linear fit. We present the final result in Fig. 5(c) and contextualize the flow dynamics with 2D slice snapshots of the simulated plume structure. Snapshot I in Fig. 5(c) ($t \approx 30$ min) marks the start of the constant mixing rate regime. Snapshot II ($t \approx 110$ min) and snapshot III ($t \approx 150$ min) are taken during the constant mixing rate period where the plume is well developed. At the tail end of the curve, snapshot IV ($t \approx 240$ min), we observe that the MEG layer has been depleted and the mixing rate decreases as the system homogenizes.

While there is an excellent match between experiment and simulation during the regime of constant mixing rate, we note that there is a more apparent mismatch at the beginning and towards the end of the convective mixing process. Here we provide possible explanations for the mismatch. In the beginning of the experiment (0–30 min), we attribute the mismatch to noise in the data, which is amplified during numerical differentiation to produce the rate of mixing [Fig. 5(c)]. During this period, the time between each tomogram is less than 1–2 min, which is significantly more resolved in time compared to the rest of the experiment (scanned every 10–20 min). The irregularity of data collection was designed to capture the early-time dynamic behavior of instability onset. However, the early-time dynamics is also known to be nonlinear and lack a well-reasoned analytical fit. Therefore, the process of numerical differentiation of the data collected during this period amplifies any small noise in the data, which results in the much noisier plot compared to the simulation. We want to point out, however, that the mismatch is mainly in the magnitude of the scalar dissipation rate; the trend of an initial increase followed by a decay is consistent between experiment and simulation. As the experiment goes on, the temporal resolution decreases to every 10–20 min. The sparsity in data sampling is not an issue during the constant flux regime ([30, 200] min). However, the decreased temporal resolution may be responsible for the mismatch between experiment and simulation towards the end (>200 min). In particular, the convective shutdown regime of the experiment appears to begin earlier and decay faster compared to the simulation [Fig. 5(c)]. This entire regime, however, is only captured by four experimental data points. Therefore, we hypothesize that the poor temporal resolution during the shutdown regime could explain the mismatch during the period $t \in [200, 275]$ min.

C. Quantifying the dissolution flux

The temporal dynamics of $\langle \epsilon' \rangle$ closely tracks the temporal dynamics of dissolution flux F [6]. As evidenced in Fig. 5(c), the time series of $\langle \epsilon' \rangle$ obtained in our experiment and simulation both exhibit the well-established three-stage progression of F [26,50]: (i) onset of instability for $t \in [0, 30)$ min, (ii) constant flux during $t \in [30, 200]$ min, and (iii) convective shutdown for $t \in [200, 275]$ min. To directly calculate F, however, one often resorts to actively tracking the volume of the overlying

fluid that remains to be dissolved [20]. This requires locating the interface with sufficient precision by image segmentation, which is prone to errors introduced by CT scanning and image processing. Here, we demonstrate an alternative approximation of the flux directly from the global measure of the scalar dissipation rate, and we avoid the need for interface tracking. In particular, we illustrate the robustness of the mixing-based flux calculation by comparing it against flux calculated from the commonly used interface-based method.

In both calculation methods shown below, we will first directly calculate the dimensionless dissolution flux, F', and then convert to dimensional units by scaling with the characteristic flux F_c:

$$F = F_c F'. \tag{8}$$

We introduce the following characteristic scales. The characteristic velocity based on the experimental parameters is calculated as

$$U_c = \frac{\Delta \rho_{\max} g k}{\mu} = \frac{9.3 \text{ kg/m}^3 \times 9.8 \text{ m/s}^2 \times 1.9 \times 10^{-10} \text{ m}^2}{1.09 \times 10^{-3} \text{ Pa s}} \approx 0.095 \text{ cm/min}. \tag{9}$$

The corresponding characteristic time is

$$t_c = \frac{\phi H_B}{U_c} = \frac{0.36 \times 13 \text{ cm}}{0.095 \text{ cm/min}} \approx 50 \text{ min}. \tag{10}$$

Note that here, the theoretical characteristic timescale of $t_c = 50$ min is slightly larger than the actual time scale ($t_{\text{scale}} = 40$ min) used to convert our dimensionless simulations results [see Fig. 5 and the discussion after Eq. (7)]. This suggests that the actual permeability of the experiments could be higher than the estimated value using the Kozeny-Carman equation. However, the exact value of t_c does not impact the calculations below because the t_c parameter cancels out in the final formulas.

We compute the characteristic flux F_c as

$$F_c = \frac{H_B^2 \rho_0 U_c / \phi}{WL} = \frac{13 \text{ cm} \times 13 \text{ cm} \times 1.04 \text{ g/mL} \times 0.265 \text{ cm/min}}{15^2 \text{ cm}^2} = 0.207 \text{ g/cm}^2/\text{min}. \tag{11}$$

1. Flux calculation based on interfacial velocity

We first obtain F in the traditional way by tracking the location of the bottom interface of the MEG layer and computing its interfacial velocity. We assume a simple picture of the convective mixing in a cubic domain where the interface moves at a constant velocity v_i during the stage of constant-rate dissolution. During this stage, the dissolution flux (F) is defined as the rate of mass exchange across a unit area, and it can be computed as a function of the velocity (v_i) of the upward-moving interface between the MEG solution and MEG-free brine:

$$F = WL\phi \rho_1 v_i, \tag{12}$$

where W and L are the width and depth of the domain (Fig. 1).

To obtain v_i in the above formula, we define the MEG layer as voxels where $c' > 0.95$, and we use image segmentation to track its bottom position $l_{\text{interface}}$ in both experimental and simulation data. Figure 8 (inset) shows the average $l_{\text{interface}}$ over time, where the linear portions of the curves correspond to the constant flux regime. We calculate the interfacial velocity as $v_i = dl_{\text{interface}}/dt$. In particular, we use a moving average filter with a six-point window to smooth the interface position data before calculating its derivative. We then convert v_i into its dimensionless form v_i' by scaling it with U_c [Eq. (9)]. Finally, we obtain the interface-based flux, F_{v_i}, using Eq. (13):

$$F_{v_i} = F_c F_{v_i}' = F_c W' L' \phi \rho_1' v_i', \tag{13}$$

where $W' = W/H_B = 1.15$, $L' = L/H_B = 1.15$, and $\rho_1' = \rho_1/\rho_0 \approx 0.99$.
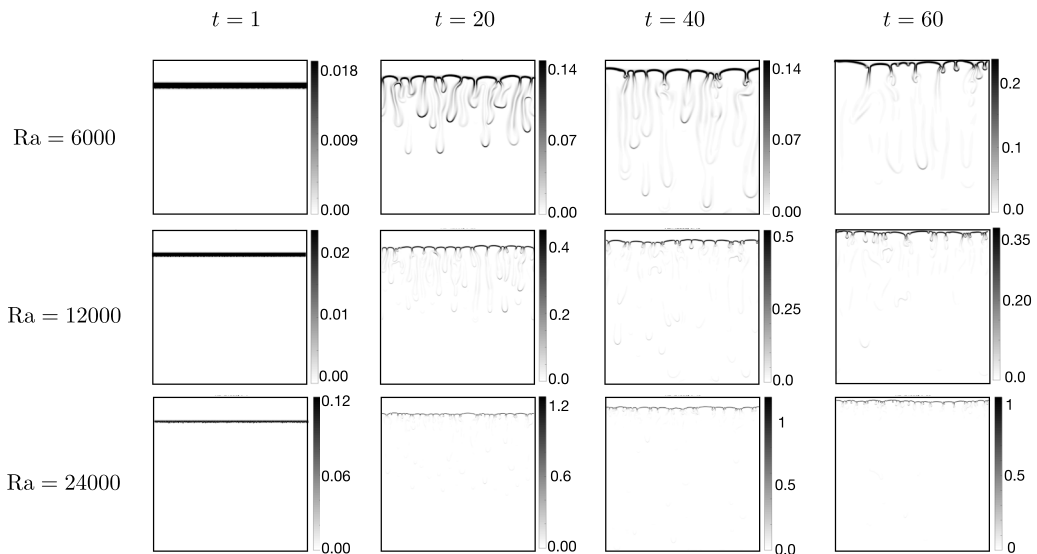
FIG. 6. In 2D, at three different Ra (row), snapshot of $\epsilon = |\nabla c|^2/\mathrm{Ra}$ obtained from the numerical simulation at four different times (column). The color map is truncated at $\epsilon_{\mathrm{threshold}} = 0.1\max(\epsilon)$ to accentuate the mixing volume (the black region).

2. Flux calculation based on scalar dissipation rate

Now, we also derive an $\langle\epsilon'\rangle$-based method to calculate flux. The volume integral of the scalar dissipation rate ϵ is computed as

$$\int_\Omega \epsilon\, dV = \int_\Omega \phi D|\nabla c|^2 dV = WL\int_{z_i(t)}^{z_i(t)+l} \phi D\left(\frac{dc}{dz}\right)^2 dz \approx WL\phi D\frac{\rho_1^2}{l}, \tag{14}$$

where l is the thickness of the interface. Equation (14) is based on two assumptions: (i) the majority of the mixing takes place within the interfacial region (across l); (ii) the concentration gradient within this region can be approximated as

$$\frac{dc}{dz} \approx \frac{c_2 - c_1}{l} = \frac{\rho_1\chi_1 - \rho_2\chi_2}{l} = -\frac{\rho_1}{l}, \tag{15}$$

with $\chi_1 \equiv 1$, $\chi_2 \equiv 0$. To support the first assumption above, we have performed additional simulations in 2D and computed the pointwise $\epsilon = |\nabla c|^2/\mathrm{Ra}$ field in both 2D and 3D simulations at different Rayleigh numbers. The results, shown in Figs. 6 and 7, confirm that the majority of the mixing volume is indeed concentrated along the interface. We further propose that the thickness of this interface, l, is maintained by a balance between diffusion and advection. Thus, l can be defined with either the diffusion or advection scaling as

$$l = \sqrt{Dt_c^l}\,(\text{diffusion scaling}), \quad l = t_c^l v_i\,(\text{advection scaling}),$$

where t_c^l is the characteristic time associated with $l_{\mathrm{diff.}}$. Equating the above two scalings yields
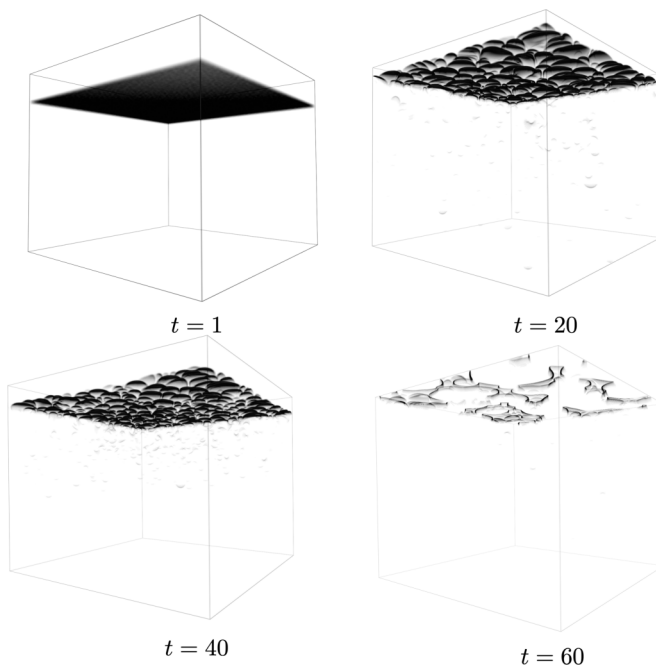
$$l = \frac{D}{v_i}. \tag{16}$$

FIG. 7. In 3D, at Ra = 6000, snapshot of $\epsilon = |\nabla c|^2/$Ra obtained from the numerical simulation at four different times. The color map is truncated at $\epsilon_{\text{threshold}} = 0.1\max(\epsilon)$ to accentuate the mixing volume (the black region).

Incorporating Eq. (16) into Eqs. (15) and (14) yields

$$\int_\Omega \epsilon \, dV \approx WL\phi \, D \frac{\rho_1^2}{D/v_i} = (WL\phi\rho_1 v_i)\rho_1. \tag{17}$$

Applying the original definition of flux in Eq. (12) to the above yields the following relationship between the actual flux F and the total volume of mixng $\int_\Omega \epsilon \, dV$:

$$F = \frac{1}{\rho_1}\int_\Omega \epsilon \, dV. \tag{18}$$

As result, we arrive at an $\langle\epsilon'\rangle$-based method to quantify the flux without actively tracking the MEG-brine interface through the following relation:

$$F_\epsilon = F_c F'_\epsilon = F_c \frac{1}{\rho'_1}\int_\Omega \epsilon' \, dV, \tag{19}$$

where $\epsilon' = |\nabla'c'|^2/$Ra is the dimensionless scalar dissipation rate, with ∇' being the normalized gradient by H_B (as introduced in Sec. III B).

3. Comparison of the two methods

We apply the above two methods to both the experimental and numerical data to compute the flux F, and we find that the interface-based method using Eq. (13) (Fig. 8, red diamonds and solid line) and the $\langle\epsilon'\rangle$-based method using Eq. (19) (Fig. 8, black diamonds and dashed line) are in very good agreement. This suggests that $\langle\epsilon'\rangle$ may serve as a direct measurement of the rate of dissolution in this problem during the quasi-steady-state regime.
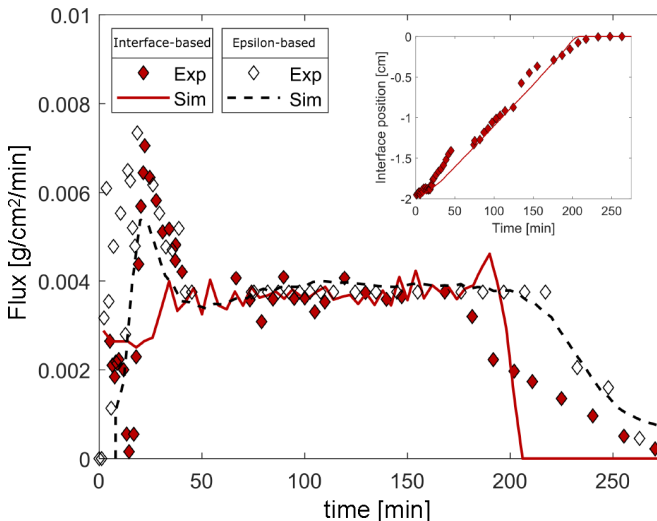
FIG. 8. Time evolution of the dissolution flux using the interface-based method (red marker), and the $\langle \epsilon' \rangle$-based method (black marker) applied to the experimental (diamonds) and simulation (lines) data. Inset: The time evolution of the interface position for the experiment (diamonds) and simulation (line).

Further, we note that these two methods agree especially well during periods where the interface remains sharp (e.g., $t \in [0, 180]$ min in Fig. 8; see also snapshots I–III in Fig. 5). This is evident from the strong overlap between red-diamond and white-diamond symbols in Fig. 8. Such an observation is consistent with a major assumption of the $\langle \epsilon' \rangle$-based method, which is that the mixing takes place within a narrow interfacial region (characterized by l). As the domain becomes increasingly well mixed, this assumption will slowly break down as the interface becomes less well defined (e.g., snapshots IV in Fig. 5), and the two methods diverge significantly during the convective shutdown regime ($t > 200$ min in Fig. 8).

IV. DISCUSSION

In comparison to the actual mass of MEG used in the experiment ($=157.9$ g), the mass obtained by integrating the flux with time in Fig. 8 is 159.3 g for the experiment (a difference of 0.84%) and 161.4 g for the simulation (a difference of 2.1%). Our approach proves to be robust and yields a mass conservation consistent with experimental calibration. Further, we note that the dimensionless flux quantified by the Sherwood number $Sh = F/(\phi \Delta c D_m / H_B)$ (with $\Delta c = 1$ g/cm^3) is $\sim$240 in this 3D experiment, compared to $Sh = 178$ from an earlier 2D experiment with similar Ra and fluid pair [20]. This suggests that experimentally measured flux in 3D is 34% higher than 2D flux. This increase in 3D flux by 34% is consistent with earlier simulation studies using the canonical setting where a fixed concentration is prescribed at the top of the domain [41,43], which have shown that 2D and 3D fluxes differ by approximately 30%. The discrepancy between 2D and 3D flux also exists in the measure using the scalar dissipation rate ϵ. In particular, the dimensionless ϵ plateaus around $\epsilon_{3D} = 0.009 - 0.01$ in our study [Fig. 5(c)], which is approximately a 28–42% increase compared to the reported 2D value of $\epsilon_{2D} \approx 0.007$ for the analog system in [6]. In the context of the body of simulation work referred to here, our work provides robust experimental confirmation of this numerical prediction of flux increase in 3D. However, we note that the exact percentage value of 3D flux increase reported here bears uncertainty. Obtaining a more accurate estimate of this flux increase requires more accurate measurements, ideally with more decimal precision in the measured concentration. We also note here that comparing fluid pairs with similar properties is important because it has been shown both experimentally [37] and numerically [6] that for a fixed

Ra (calculated with the viscosity of the resident fluid), the mixing rate and by extension Sh is weakly dependent on the viscosity ratio.

The effect of mechanical dispersion can also significantly impact the dynamics of convective mixing. In particular, increased mechanical dispersion can (i) modify the finger structure by promoting coalescence of adjacent fingers [21,49]; (ii) decrease the onset time by enhancing the mixing at the initial interface [14,49]; and (iii) reduce the dissolution flux by reducing the concentration gradients and thus the strength of convection [11,14]. Such effects of dispersion are expected to be most prominent in a coarse medium where the average grain diameter $d_p > 0.4$ mm [12,21]. This threshold is most pertinent for granular porous media, such as that used in this work, and originally was verified in a 2D system. Although we do not consider mechanical dispersion in our numerical model, encouragingly we still find good agreement between experiment and simulation in all aspects of our analysis. We hypothesize that this is due to the value of the average bead diameter used in our experiment, which lies exactly on the threshold around $d_p = 0.4-0.5$ mm where mechanical dispersion becomes important. Given that our experimental system sits at the coarseness threshold where pore-scale dynamics may not be readily captured by REV-scale homogenization, we also calculate the pore-scale Reynolds number in our experiment as [60]

$$\text{Re} = \frac{\rho_0 U_c \sqrt{k}}{\mu} \approx 0.21 \times 10^{-3} \ll 1, \tag{20}$$

which suggests that inertia should be negligible. Similarly, the pore-scale Péclet number, defined as the ratio between pore size scale and the natural length scale (l) [60], is calculated as

$$\text{Pe} = \frac{\sqrt{k}}{l} \approx 0.57 < 1, \tag{21}$$

where $l = \phi D_m / U_c \approx 2.27 \times 10^{-5}$ m. This suggests that the lengthscale of the boundary layer spans only a few pores in size in our experiment.

We expect that the analysis performed here will also be robust for even finer bead sizes (lower permeability), which are representative analogs to the field reported, e.g., in the United States [61,62] and the Sleipner site in the North Sea [63], where geologic carbon sequestration is being actively explored. However, in extending the conclusions of this work to geologic porous formations, we note that the homogeneous glass bead pack we use in our experiments may not capture the complexity of geologic porous media that have a heterogeneous pore structure and thus more complicated dispersion effects.

Our work reports a direct comparison between experiments and simulations of density-driven mixing in a 3D porous media. The success of this comparison study also represents an important step forward as it demonstrates that direct validation of quantitative imaging in 3D porous media against simulations is possible. This enables future experimental investigations on the role of other parameters not considered in this study, and paves the way for direct translation of experimental results into modeling the physical process of convective mixing in 3D.

The data that support the findings of this study can be found in the Caltech Data Library [64] or are available from the corresponding author upon reasonable request.

[1] B. Gebhart and L. Pera, The nature of vertical natural convection flows resulting from the combined buoyancy effects of thermal and mass diffusion, Int. J. Heat Mass Transf. **14**, 2025 (1971).

[2] P. Cheng, *Heat Transfer in Geothermal Systems* (Elsevier, Amsterdam, 1979), pp. 1–105.

[3] J. Ennis-King and L. Paterson, Role of convective mixing in the long-term storage of carbon dioxide in deep saline formations, SPE J. **10**, 349 (2005).

[4] H. Emami-Meybodi, H. Hassanzadeh, C. P. Green, and J. Ennis-King, Convective dissolution of CO_2 in saline aquifers: Progress in modeling and experiments, Int. J. Greenhouse Gas Contr. **40**, 238 (2015).

[5] A. C. Slim and T. S. Ramakrishnan, Onset and cessation of time-dependent, dissolution-driven convection in porous media, Phys. Fluids **22**, 124103 (2010).

[6] J. J. Hidalgo, J. Fe, L. Cueto-Felgueroso, and R. Juanes, Scaling of convective mixing in porous media, Phys. Rev. Lett. **109**, 264503 (2012).

[7] A. C. Slim, Solutal-convection regimes in a two-dimensional porous medium, J. Fluid Mech. **741**, 461 (2014).

[8] A.-M. Eckel and R. Pini, Spreading and mixing during solutal convection in uniform porous media with application to geologic CO_2 storage, Phys. Fluids **33**, 066604 (2021).

[9] S. M. Jafari Raad and H. Hassanzadeh, Onset of dissolution-driven instabilities in fluids with nonmonotonic density profile, Phys. Rev. E **92**, 053023 (2015).

[10] S. M. Jafari Raad, H. Emami-Meybodi, and H. Hassanzadeh, On the choice of analogue fluids in CO_2 convective dissolution experiments, Water Resour. Res. **52**, 4458 (2016).

[11] K. Ghesmat, H. Hassanzadeh, and J. Abedi, The effect of anisotropic dispersion on the convective mixing in long-term CO_2 storage in saline aquifers, AIChE J. **57**, 561 (2011).

[12] B. Wen, K. W. Chang, and M. A. Hesse, Rayleigh-Darcy convection with hydrodynamic dispersion, Phys. Rev. Fluids **3**, 123801 (2018).

[13] H. Emami-Meybodi, Dispersion-driven instability of mixed convective flow in porous media, Phys. Fluids **29**, 094102 (2017).

[14] J. J. Hidalgo and J. Carrera, Effect of dispersion on the onset of convection during CO_2 sequestration, J. Fluid Mech. **640**, 441 (2009).

[15] M. T. Elenius and S. E. Gasda, Convective mixing in formations with horizontal barriers, Adv. Water Resour. **62**, 499 (2013).

[16] C. Green and J. Ennis-King, Steady flux regime during convective mixing in three-dimensional heterogeneous porous media, Fluids **3**, 58 (2018).

[17] S. Backhaus, K. Turitsyn, and R. E. Ecke, Convective instability and mass transport of diffusion layers in a Hele-Shaw geometry, Phys. Rev. Lett. **106**, 104501 (2011).

[18] C. Thomas, L. Lemaigre, A. Zalts, A. D'Onofrio, and A. De Wit, Experimental study of CO_2 convective dissolution: The effect of color indicators, Int. J. Greenhouse Gas Contr. **42**, 525 (2015).

[19] M. De Paoli, M. Alipour, and A. Soldati, How non-darcy effects influence scaling laws in hele-shaw convection experiments, J. Fluid Mech. **892**, A41 (2020).

[20] J. A. Neufeld, M. A. Hesse, A. Riaz, M. A. Hallworth, H. A. Tchelepi, and H. E. Huppert, Convective dissolution of carbon dioxide in saline aquifers, Geophys. Res. Lett. **37**, 2010GL044728 (2010).

[21] Y. Liang, B. Wen, M. A. Hesse, and D. DiCarlo, Effect of dispersion on solutal convection in porous media, Geophys. Res. Lett. **45**, 9690 (2018).

[22] E. Agartan, L. Trevisan, A. C. J., B. Q. Zhou, and T. Illangasekare, Experimental study on effects of geologic heterogeneity in enhancing dissolution trapping of supercritical CO_2, Water Resour. Res. **51**, 1635 (2015).

[23] P. A. Tsai, H. Riesing, and H. A. Stone, Density-driven convection enhanced by an inclined boundary: Implications for geological CO_2 storage, Phys. Rev. E **87**, 011003(R) (2013).

[24] C. W. Macminn and R. Juanes, Buoyant currents arrested by convective dissolution, Geophys. Res. Lett. **40**, 2017 (2013).

[25] T. J. Kneafsey and K. Pruess, Laboratory flow experiments for visualizing carbon dioxide-induced, density-driven brine convection, Transp. Porous Media **82**, 123 (2010).

[26] A. C. Slim, M. M. Bandi, J. C. Miller, and L. Mahadevan, Dissolution-driven convection in a Hele–Shaw cell, Phys. Fluids **25**, 024101 (2013).

[27] J.-H. Ching, P. Chen, and P. A. Tsai, Convective mixing in homogeneous porous media flow, Phys. Rev. Fluids **2**, 014102 (2017).

[28] S. Mahmoodpour, M. A. Amooie, B. Rostami, and F. Bahrami, Effect of gas impurity on the convective dissolution of CO_2 in porous media, Energy **199**, 117397 (2020).

[29] S. Mahmoodpour, B. Rostami, M. R. Soltanian, and M. A. Amooie, Convective dissolution of carbon dioxide in deep saline aquifers: Insights from engineering a high-pressure porous visual cell, Phys. Rev. Appl. **12**, 034016 (2019).

[30] S. Mahmoodpour, B. Rostami, M. R. Soltanian, and M. A. Amooie, Effect of brine composition on the onset of convection during CO_2 dissolution in brine, Comput. Geosci. **124**, 1 (2019).

[31] D. L. Newell, J. W. Carey, S. N. Backhaus, and P. Lichtner, Experimental study of gravitational mixing of supercritical CO_2, Int. J. Greenhouse Gas Contr. **71**, 62 (2018).

[32] Z. Shi, B. Wen, M. Hesse, T. Tsotsis, and K. Jessen, Measurement and modeling of CO_2 mass transfer in brine at reservoir conditions, Adv. Water Resour. **113**, 100 (2018).

[33] E. Agartan, T. H. Illangasekare, J. Vargas-Johnson, A. Cihan, and J. Birkholzer, Experimental investigation of assessment of the contribution of heterogeneous semi-confining shale layers on mixing and trapping of dissolved CO_2 in deep geologic formations, Int. J. Greenhouse Gas Contr. **93**, 102888 (2020).

[34] A. Taheri, O. Torsæter, E. Lindeberg, N. J. Hadia, and D. Wessel-Berg, Qualitative and quantitative experimental study of convective mixing process during storage of CO_2 in heterogeneous saline aquifers, Int. J. Greenhouse Gas Contr. **71**, 212 (2018).

[35] L. Wang, Y. Nakanishi, A. Hyodo, and T. Suekane, Three-dimensional structure of natural convection in a porous medium: Effect of dispersion on finger structure, Int. J. Greenhouse Gas Contr. **53**, 274 (2016).

[36] R. Liyanage, J. Cen, S. Krevor, J. P. Crawshaw, and R. Pini, Multidimensional observations of dissolution-driven convection in simple porous media using X-ray CT scanning, Transp. Porous Med. **126**, 355 (2019).

[37] R. Liyanage, A. Russell, J. P. Crawshaw, and S. Krevor, Direct experimental observations of the impact of viscosity contrast on convective mixing in a three-dimensional porous medium, Phys. Fluids **32**, 056604 (2020).

[38] S. Wang, Z. Cheng, L. Jiang, Y. Song, and Y. Liu, Quantitative study of density-driven convection mass transfer in porous media by MRI, J. Hydrol. **594**, 125941 (2021).

[39] A.-M. Eckel, R. Liyanage, T. Kurotori, and R. Pini, Spatial moment analysis of convective mixing in three-dimensional porous media using X-ray CT images, Ind. Eng. Chem. Res. **62**, 762 (2023).

[40] S. Sin, S. Imai, M. A. Mahardika, A. Patmonoaji, M. Nasir, W. Susanto, S. Matsushita, and T. Suekane, Three-dimensional visualization of Rayleigh–Bénard convection in porous media, Adv. Water Resour. **186**, 104666 (2024).

[41] G. S. H. Pau, J. B. Bell, K. Pruess, A. S. Almgren, M. J. Lijewski, and K. Zhang, High-resolution simulation and characterization of density-driven flow in CO_2 storage in saline aquifers, Adv. Water Resour. **33**, 443 (2010).

[42] X. Fu, L. Cueto-Felgueroso, D. Bolster, and R. Juanes, Rock dissolution patterns and geochemical shutdown of CO_2–brine–carbonate reactions during convective mixing in porous media, J. Fluid Mech. **764**, 296 (2015).

[43] X. Fu, L. Cueto-Felgueroso, and R. Juanes, Pattern formation and coarsening dynamics in three-dimensional convective mixing in porous media, Philos. Trans. A **371**, 20120355 (2013).

[44] P. Fruton, A. Nauruzbaeva, H. Bataller, C. Giraudet, A. Vailati, and F. Croccolo, Convective dissolution of carbon dioxide into brine in a three-dimensional free medium, Phys. Rev. Fluids **8**, 023503 (2023).

[45] M. R. Soltanian, M. A. Amooie, N. Gershenzon, Z. Dai, R. Ritzi, F. Xiong, D. Cole, and J. Moortgat, Dissolution trapping of carbon dioxide in heterogeneous aquifers, Environ. Sci. Technol. **51**, 7732 (2017).

[46] M. A. Amooie, M. R. Soltanian, and J. Moortgat, Solutal convection in porous media: Comparison between boundary conditions of constant concentration and constant flux, Phys. Rev. E **98**, 033118 (2018).

[47] S. Pirozzoli, M. De Paoli, F. Zonta, and A. Soldati, Towards the ultimate regime in Rayleigh–Darcy convection, J. Fluid Mech. **911**, R4 (2021).

[48] M. De Paoli, S. Pirozzoli, F. Zonta, and A. Soldati, Strong Rayleigh–Darcy convection regime in three-dimensional porous media, J. Fluid Mech. **943**, A51 (2022).

[49] L. Wang, Y. Nakanishi, A. D. Teston, and T. Suekane, Effect of diffusing layer thickness on the density-driven natural convection of miscible fluids in porous media: Modeling of mass transport, J. Fluid Sci. Technol. **13**, JFST0002 (2018).

[50] A. Riaz, M. Hesse, H. A. Tchelepi, and F. M. Orr, Jr., Onset of convection in a gravitationally unstable diffusive boundary layer in porous media, J. Fluid Mech. **548**, 87 (2006).

[51] G. Ternström, A. Sjöstrand, G. Aly, and Å. Jernqvist, Mutual diffusion coefficients of water + ethylene glycol and water + glycerol mixtures, J. Chem. Eng. Data **41**, 876 (1996).

[52] C. T. Tan and G. M. Homsy, Simulation of nonlinear viscous fingering in miscible displacement, Phys. Fluids **31**, 1330 (1988).

[53] A. Riaz and E. Meiburg, Three-dimensional miscible displacement simulations in homogeneous porous media with gravity override, J. Fluid Mech. **494**, 95 (2003).

[54] P. N. Swarztrauber, The methods of cyclic reduction, Fourier analysis, and the FACR algorithm for the discrete solution of Poisson's equation on a rectangle, SIAM Rev. **19**, 490 (1977).

[55] S. K. Lele, Compact finite difference methods with spectral-like resolution, J. Comput. Phys. **103**, 16 (1992).

[56] M. Ruith and E. Meiburg, Miscible rectilinear displacements with gravity override. Part 1. Homogeneous porous medium, J. Fluid Mech. **420**, 225 (2000).

[57] B. Jha, L. Cueto-Felgueroso, and R. Juanes, Fluid mixing from viscous fingering, Phys. Rev. Lett. **106**, 194502 (2011).

[58] B. Jha, L. Cueto-Felgueroso, and R. Juanes, Quantifying mixing in viscously unstable porous media flows, Phys. Rev. E **84**, 066312 (2011).

[59] S. B. Pope, *Turbulent Flows* (Cambridge University Press, Cambridge, England, 2000).

[60] M. De Paoli, Convective mixing in porous media: a review of Darcy, pore-scale and Hele-Shaw studies, Eur. Phys. J. E **46**, 129 (2023).

[61] M. L. Szulczewski, C. W. MacMinn, H. J. Herzog, and R. Juanes, Lifetime of carbon capture and storage as a climate-change mitigation technology, Proc. Natl. Acad. Sci. USA **109**, 5185 (2012).

[62] H. Hassanzadeh, M. Pooladi-Darvish, and D. W. Keith, Scaling behavior of convective mixing, with application to geological storage of CO_2, AIChE J. **53**, 1121 (2007).

[63] K. J. Sathaye, M. A. Hesse, M. Cassidy, and D. F. Stockli, Constraints on the magnitude and rate of CO_2 dissolution at Bravo Dome natural gas field, Proc. Natl. Acad. Sci. USA **111**, 15332 (2014).

[64] X. Fu, Data used in "Direct comparison of density-driven mixing in a three-dimensional porous media using experiments and simulation," CaltechDATA 10.22002/n1mdr-zd551 (2024).